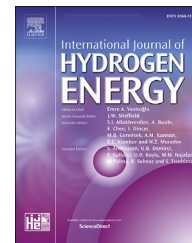




ELSEVIER

Available online at www.sciencedirect.com

ScienceDirect

journal homepage: www.elsevier.com/locate/he

Microstructure optimization of nickel/gadolinium-doped ceria anodes as key to significantly increasing power density of metal-supported solid oxide fuel cells

Cornelia Bischof^{a,b,*}, Andreas Nenning^{a,c}, Andreas Malleier^b,
Lukas Martetschläger^b, Andre Gladbach^b, Wolfgang Schafbauer^b,
Alexander K. Opitz^{a,c}, Martin Bram^{a,d}

^a Christian Doppler Laboratory for Interfaces in Metal-Supported Electrochemical Energy Converters, 52425, Jülich, Germany

^b Plansee SE, Corporate Research & Development, 6600, Reutte, Austria

^c TU Wien, Institute of Chemical Technologies and Analytics, Getreidemarkt 9/164-EC, 1060, Vienna, Austria

^d Forschungszentrum Jülich GmbH, Institute of Energy and Climate Research, Materials Synthesis and Processing (IEK-1), 52425, Jülich, Germany

HIGHLIGHTS

- Cell performance +38% by microstructure optimization of three-layered anode.
- Ni/GDC in the anode interlayer clearly extends electrochemically active region.
- Anode properties defined as keys for reliable electrolyte processing.
- Thickness of gas-flow sputtered electrolyte successfully reduced from 4 μm to 2 μm.

ARTICLE INFO

Article history:

Received 15 July 2019

Received in revised form

24 September 2019

Accepted 4 October 2019

Available online 31 October 2019

Keywords:

Solid oxide fuel cell

Metal-support

Microstructure

Ni/GDC anode

ABSTRACT

Metal-supported solid oxide fuel cells (MSCs) are promising candidates for mobile power generators like range extenders for battery electric vehicles due to their improved thermal conductivity and ruggedness. The limited space available in such vehicles heightens the need to achieve high power densities. In the present study, a significant increase in cell performance of the MSC concept of Plansee SE was demonstrated by means of systematic microstructure optimization of the complete cell architecture based on improved processing. Thickness and roughness of multi-layered Ni/GDC anode play a particularly important role in improving cell performance. After several optimization steps, a notable increase of current density from 1.29 A/cm² to 1.79 A/cm² at 700 °C and 0.7 V (+38%) was achieved. Additionally, lowering the anode roughness enables clear reduction of electrolyte thickness down to 2 μm, a starting point for the further enhancement of cell performance.

© 2019 Hydrogen Energy Publications LLC. Published by Elsevier Ltd. All rights reserved.

* Corresponding author. Plansee SE, Corporate Research & Development, 6600, Reutte, Austria.

E-mail address: c.bischof@fz-juelich.de (C. Bischof).

<https://doi.org/10.1016/j.ijhydene.2019.10.010>

0360-3199/© 2019 Hydrogen Energy Publications LLC. Published by Elsevier Ltd. All rights reserved.

Introduction

Solid oxide fuel cells (SOFCs) provide an efficient means of converting fuel directly into electrical energy. Recent progress in SOFC technology includes metal-supported fuel cells (MSCs), which offer advantages with regard to rapid thermal cycles, mechanical stability and compatibility with the surrounding metal housing. However, further developments are crucial in order to achieve the primary target of integration in an MSC-based power generator for the commercial mobile applications. Promising applications for such a power generator include auxiliary power units (APUs) in trucks [1] and SOFC-based range extender systems for battery electric vehicles (BEVs), which enable battery packs to be recharged without the need for external electrical power [2]. A prototype SOFC range extender developed by AVL List GmbH, Austria, is used in the Nissan e-NV200 SOFC vehicle, it provides an electrical power of 5 kW and is operated preferentially with bioethanol [3]. When integrating the generator in a vehicle, limitations regarding both weight and volume of the SOFC stack and balance of plant components including a fuel tank have to be considered. Therefore, research groups have been working for more than a decade on significantly increasing the power density of MSCs.

The main MSC concepts differ clearly in cell architecture and cell processing. In the following section, the main MSC concepts are introduced. A general issue of MSC manufacturing is the need to protect the metal substrate from strong oxidation, which requires low oxygen partial pressures or low temperatures during the processing of the electrolyte and electrodes.

The MSC concept of the British company Ceres Power [4,5] aims on operation at intermediate temperature in the range of 500–600 °C. As substrate, a 200 μm thick perforated sheet made of Ti- and Nb-stabilized steel with 17% Cr is used. The anode consists of a wet-sprayed or screen-printed Ni/GDC (gadolinium-doped ceria, $\text{Ce}_{0.9}\text{Gd}_{0.1}\text{O}_{2-\delta}$) cermet. The three-layered, 10–30 μm thick electrolyte is deposited by electrophoretic deposition. It combines a GDC-layer on the anode, followed by an YSZ electron-blocking layer and another GDC layer, which acts as diffusion-barrier layer to protect YSZ from reaction with LSCF ($\text{La}_{1-x}\text{Sr}_x\text{Co}_{1-y}\text{Fe}_y\text{O}_{3-\delta}$) in the LSCF/GDC composite cathode. A current density of 0.25 A/cm² was reported at an operating temperature of 550 °C and a cell voltage of 0.7 V. The active area was 16 cm².

In the group of Tucker at Lawrence Berkeley National Laboratory, USA [6,7] a symmetrical MSC concept is under development. This concept is based on laminated tape-cast layers and infiltrated electrodes. A 200 μm thick stainless steel served as metal substrate. Recently, highly conductive SCSZ (10Sc1CeSZ) was implemented for the 7 μm thick electrolyte. Ni/SDC ($\text{Sm}_{0.2}\text{Ce}_{0.8}\text{O}_{2-\delta}$) and Pr_6O_{11} are used as anode and cathode materials. A current density up to 2.2 A/cm² was achieved at 700 °C, 0.7 V on an active area of 1 cm². Long term stability is one of the challenging tasks if applying infiltrated electrodes due to the risk of coarsening the nanostructured catalysts.

Nielsen et al. at DTU, Danmark [8,9] developed a MSC concept based on laminated tape-cast layers, an infiltrated Ni/

GDC anode and a screen-printed LSC cathode. The substrate is made from a FeCr22 alloy powder with a thickness of 240 μm. The anode backbone consists of Y-doped ZrO_2 . ScYSZ serves as electrolyte with a thickness of 9 μm. The adjacent GDC10 diffusion barrier layer is deposited by physical vapor deposition. A current density of 1.44 A/cm² was achieved at 700 °C, 0.7 V and an active cell area of 16 cm².

Li et al. from Huazhong University of Science & Technology, China [10] produced MSCs by screen-printing of all active layers on 1 mm thick Ni–Fe-alloy substrates. Ni/GDC is used as anode and GDC as electrolyte material. Electrolyte thickness is 10 μm and anode thickness is 15 μm. LSM-BSCF ($\text{La}_{0.8}\text{Sr}_{0.2}\text{MnO}_3\text{--Ba}_{0.5}\text{Sr}_{0.5}\text{Co}_{0.2}\text{Fe}_{0.8}\text{O}_3$) served as cathode material. The current density at 700 °C was 0.55 A/cm² on an active cell area of 0.5 cm².

Zhou et al. from Chinese Academy of Sciences (SICCAS) [11] produced MSCs by laminating substrate, electrolyte and anode backbone layers and subsequent infiltration of catalysts. In this work, stainless steel is used for the metal substrate, which has a thickness of 300 μm. YSZ serves as material for the 30 μm thick electrolyte. 10 wt % Ni is infiltrated as anode catalyst into the metal substrate and 30 wt % LSFsc ($\text{La}_{0.6}\text{Sr}_{0.4}\text{Fe}_{0.9}\text{Sc}_{0.1}\text{O}_{3-\delta}$) as cathode catalyst into the porous YSZ. The authors achieved a current density of 0.5 A/cm² at 700 °C (active area of 0.35 cm²).

Hwang et al. from Institute of Nuclear Energy Research, Taiwan [12] produced MSCs by a plasma spraying. A Ni/Mo-substrate is covered by a LSCM diffusion barrier layer ($\text{La}_{0.75}\text{Sr}_{0.25}\text{Cr}_{0.5}\text{Mn}_{0.5}\text{O}_{3-\delta}$), a Ni-LDC anode ($\text{Ce}_{0.55}\text{La}_{0.45}\text{O}_{2-\delta}$), a LSGM electrolyte ($\text{La}_{0.8}\text{Sr}_{0.2}\text{Ga}_{0.8}\text{Mg}_{0.2}\text{O}_{3-\delta}$) and an SSC cathode ($\text{Sm}_{0.5}\text{Sr}_{0.5}\text{CoO}_{3-\delta}$). The anode thickness is 20–40 μm and the electrolyte thickness 40–50 μm. In this work, a current density of 1.4 A/cm² at 700 °C, 0.8 V and an active cell size of 16 cm² was reported. A detailed overview of all existing MSC concepts can be found in two review articles [13,14].

The MSC concept developed by Plansee SE, Austria, is based on a highly porous metallic substrate [15]. Contrary to other existing cell concepts, a three-layered anode is deposited by screen printing and sintered under a reducing hydrogen atmosphere, followed by gas flow sputtering of the electrolyte and ex-situ sintering of a screen-printed cathode. To avoid excessive inter-diffusion at the interfaces, diffusion barrier layers formed by physical vapor deposition (PVD) are placed between the metal substrate and the anode as well as between the electrolyte and the cathode. Fig. 1 shows the cell architecture of the Plansee MSC concept in detail.

In the three anode layers, pore size is progressively reduced to enable a thin-film electrolyte with a thickness of less than 5 μm to be deposited. Details of cell processing can be found in other studies [16]. In the recent work of Rojek-Wöckner et al., Ni/GDC (nickel/gadolinium-doped ceria) was introduced as a material for the top-most anode layer (denoted “C” in Fig. 1), replacing the well-established Ni/YSZ (nickel/yttrium-doped zirconia) anode [17]. It was found that introducing GDC into the composite anode clearly increased cell performance. This improvement is a result of the increased electrochemically active area due to the mixed ionic and electronic conductivity of GDC under reducing

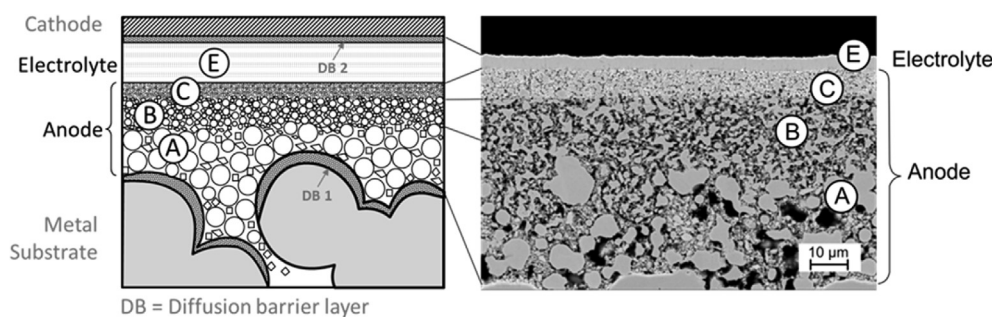


Fig. 1 – Cell architecture of the Plansee MSC.

conditions [18]. The thickness of the Ni/GDC anode layer was varied between 3 and 9 μm , but no final conclusion as to the optimum thickness of the electrochemically active area has been drawn. Up to now, influence of the active thickness of Ni/GDC anodes on SOFC performance was rarely reported in the literature so far. Sumi et al. [19] varied the Ni/GDC-layer thickness between 10 and 23 μm and reached the highest current density in the case of 23 μm (operation temperature 550 $^{\circ}\text{C}$). However, no cells with higher layer thicknesses were investigated.

Several groups addressed the importance of active anode thickness [20–25]. However, different conclusions were drawn, which might be caused by the fact that there were significant differences of cell concepts, anode materials, microstructures and operating conditions.

Several models are proposed in the literature for mixed ionic and electronic conducting electrodes to estimate optimum cell architecture and thickness of electrochemically active area. Recently, the Adler-Lane-Steele model [26–28] was adapted for Ni/GDC anodes [18,29]. Related works have also been published by Nakamura et al. [30], Wu et al. [31], Dierickx et al. [32] and Chan and Xia [33], which are helpful to identify the main influence factors for achieving high performing electrodes, but systematic experimental studies are necessarily required to find the optimum conditions for a specific cell design. For improving the Plansee MSC concept, the following factors have to be taken into consideration, which are difficult to consider properly in the above-mentioned models.

- Reliable prediction of gas diffusion limitation in a multi-layered porous structure is a quite complex modelling task. Therefore, direct measuring would be advantageous.
- Optimization of sintering and processing conditions is expected to clearly improve amount of electrochemically active sites and to enable reduced electrolyte thickness, but might in worst case also lead to loss of mechanical stability and strong bending of the cells.
- Deposition of thin film electrolyte by PVD requires extremely low surface roughness of the anode layer. Surface roughness is significantly influenced by thickness of all three anode layers. Due to columnar layer growth of PVD coatings, convex curvature of anode triggers formation of interspaces between the columns, while concave

curvature supports formation of pinholes due to shadowing effects.

To face these challenges, a systematic experimental approach was conducted with the aim to find the optimum thickness and processing conditions for the three-layered anode sketched in Fig. 1. The progress of cell development was demonstrated by characterizing electrochemical performance under standardized testing conditions.

Ultimately, an improvement in cell performance of 38% was achieved.

Experimental

To systematically investigate the influencing factors described above, three series of samples were produced. In series C, the thickness of anode layer C was varied to between 4 and 24 μm , with the anode sintering temperature kept constant at 1000 $^{\circ}\text{C}$. This relatively low sintering temperature was chosen to avoid excessive coarsening of Ni during cell production. In series E, a possible way to reduce the electrolyte thickness down to 2 μm was tested. In this case, a thickness of 22 μm was chosen for anode layer C to provide minimum surface roughness. To ensure that the anode-electrolyte interface was sufficiently stable, the anode sintering temperature had to be increased to 1100 $^{\circ}\text{C}$, which in turn led to coarsening of the Ni phase. Finally, in series BC, the electrochemical activity of the anode was further improved by replacing Ni/YSZ in anode layer B with Ni/GDC. The thickness of anode layer C was kept constant at 8 μm and an overall Ni/GDC thickness of 16–30 μm in anode layers B and C was investigated. The main goal for this series was to take full advantage of GDC as an electrochemically active phase while keeping the gas permeability of the anode at a high level. In series BC, an electrolyte thickness of 4 μm was maintained to ensure sufficient gas tightness. Table 1 summarizes all parameter variations used in this study. To compare electrochemical performance, single-cell tests were conducted at button cell level under constant testing conditions. In all cases, a screen-printed LSCF cathode was applied, which was sintered *in-situ* before the cell tests.

Table 1 – Systematic variation of the Plansee MSC cell architecture to determine optimum anode thickness and processing conditions.

Reference series R [16 – Rojek-Wöckner 2016]		Series C	Series E	Series BC
Cell component	Composition	Thickness [μm]	Thickness [μm]	Thickness [μm]
Cathode	LSCF	40	n.v.	n.v.
DB 2	GDC20	0.3	n.v.	n.v.
Electrolyte	8YSZ	4	n.v.	2
Anode layer C	Ni/GDC10 60/40 wt %	8	4–24 (1000 °C)	22 (1100 °C)
Anode layer B	Ni/8YSZ 65/35 wt %	22 (1200 °C)	n.v.	n.v.
				Ni/GDC 60:40 wt % (1100 °C)
Anode layer A	Ni/8YSZ 65/35 wt %	25 (1200 °C)	n.v.	n.v.
DB 1	GDC20	0.3	n.v.	n.v.
Metal substrate	ITM: Fe26Cr(Mo,Ti,Y ₂ O ₃)	300–800	n.v.	n.v.

n.v. = not varied, DB = diffusion barrier layer.

Starting materials

The substrate material used was ferritic steel Fe–26Cr–Mo,Ti,Y₂O₃ (Plansee name “Intermediate Temperature Metal”, ITM). Substrates with an open porosity of approximately 40 vol % and an average pore size in the range of 20–60 μm were produced in-house by means of powder metallurgy. The substrates were 100 × 140 mm² in size, with thicknesses of 300 μm and 800 μm . This difference in substrate thickness was a result of their origin in different R&D projects and had – to the best of our knowledge – no impact on electrochemical performance, since the gas diffusion resistance of the metal substrate was very low compared to the anode layers A–C. Commercial Ni, GDC10, and 8YSZ powders were considered in this study. For anode layer A, coarse Ni powder (T123™ Nickel Powder (CDN), Vale, Saint-Ouen-l’Aumône) with a particle size distribution of $d_{10} = 5.25 \mu\text{m}$, $d_{50} = 12.75 \mu\text{m}$, $d_{90} = 36.14 \mu\text{m}$ and coarse YSZ powder (13 wt % Y₂O₃/ZrO₂, IMERYS) with a particle size distribution of $d_{10} = 0.52 \mu\text{m}$, $d_{50} = 1.05 \mu\text{m}$, $d_{90} = 2.73 \mu\text{m}$ were used. For anode layer B, ultrafine Ni powder of grade 0.4 μm (Toho NF41, Toho Titanium Co., Ltd.) with a particle size of $d_{10} = 0.82 \mu\text{m}$, $d_{50} = 1.23 \mu\text{m}$, $d_{90} = 2.17 \mu\text{m}$ was applied. Where anode layer B was made of Ni/YSZ, same YSZ powder as in anode layer A was used. If anode layer B was made of Ni/GDC, GDC10 powder EA35 12.2 (Treibacher Industry AG) with a particle size of $d_{10} = 0.79 \mu\text{m}$, $d_{50} = 1.72 \mu\text{m}$, $d_{90} = 3.05 \mu\text{m}$ was used. For anode layer C, ultrafine Ni powder Toho NF41 and ultrafine GDC10 powder GDC10 EA35 12.1 (Treibacher Industry AG) with a particle size of $d_{10} = 0.16 \mu\text{m}$, $d_{50} = 0.28 \mu\text{m}$, $d_{90} = 0.40 \mu\text{m}$ were used. Before measurement, the granulated powders were treated in an ultrasonic bath to destroy primary agglomerates. [Supplementary Fig. S1](#) shows the morphology of all starting powders used in this study. For gas flow sputtering of the electrolyte, the target material used was a metallic zirconium-yttrium-alloy (85.5 wt % Zr, 14.5 wt % Y).

Manufacturing of button cells

All MSCs investigated in this study were produced in accordance with the manufacturing methods published in previous studies [16,17]. With respect to the reference cell

(reference series R), as stated above, the thickness of anode layers B and C was systematically varied, YSZ was replaced with GDC10 in anode layer B, the sintering temperature in anode layer C was varied, and the electrolyte thickness was reduced (layer E). [Table 2](#) lists all button cells produced for this study. Cells were named based on their series name, i.e. R, C, E, or BC. In the case of series C and BC, the overall thickness of Ni/GDC in the anode was taken into account in the sample code, e.g. “BC23” for a cell from series BC with 15 μm Ni/GDC in anode layer B and 8 μm Ni/GDC in anode layer C (i.e. 15 + 8 = 23).

All anode layers were produced by screen printing. The amount of Ni in the anode layers was kept constant at 65 wt % in the case of Ni/YSZ and 60 wt % in the case of Ni/GDC layers. For Ni/YSZ anode layers, standard screen-printing pastes were used in accordance with previous studies [16,34,35]. For Ni/GDC anodes, pastes were produced in-house. As a first processing step, pre-suspensions of GDC10 powders (Treibacher EA35 12.2 or Treibacher EA35 12.1) in terpineol with a solid content of 79 wt % were produced. A commercial dispersion agent (Nuospense® FA196 or FX9086, Elementis Specialities, USA) was added in an amount below 1 wt %. The pre-suspensions were milled with zirconia grinding balls on a tumbling mixer for 24 h and filtrated afterwards to remove agglomerates. A binder solution was then prepared by dissolving 15 wt % ethyl cellulose 46 cp (Sigma-Aldrich) in terpineol. To prepare the paste, pre-suspension and binder solution were mixed and ultrafine nickel was added under stirring. The final homogeneity was obtained by performing four rolling steps on a three-roll mill.

Anode screen printing

For screen printing, polyester screens from Koenen were used. For anode layer A, a screen with a wet layer thickness of 69 μm was used in all cases. The screen was masked, resulting in a printing area adjusted to the substrate dimensions. For anode layer B, a screen with a wet layer thickness of 104 μm was applied in series R, C and E. In series BC, a screen with a lower wet layer thickness of 63 μm was used. Thickness variation was achieved by performing multiple screen printing cycles (1, 2, and 3 repetitions of the same printing step). For this multiple printing, the printed layer was dried at 60 °C in an oven

Table 2 – Overview of all button cells produced for this study.

Cell series	Cell ID (internal Plansee code)	B-anode, Ni amount in wt. %	B-anode thickness	B-sinter parameters	C–Ni/GDC anode thickness	C-sinter parameters	Electrolyte thickness	Substrate thickness
R	1704–029	Ni/YSZ 65% Ni	22 μm	1200 °C/3h/H ₂	8 μm	1100 °C/3h/H ₂	4 μm	0.3 mm
C4	1604–242	Ni/YSZ 65% Ni	22	1200 °C/3h/H ₂	4	1000 °C/1.5h/H ₂	4	0.8
	1604–249							
C6	1604–245	Ni/YSZ 65% Ni	22	1200 °C/3h/H ₂	6	1000 °C/1.5h/H ₂	4	0.8
	1604–246							
	1604–257							
C8	1702–012	Ni/YSZ 65% Ni	22	1200 °C/3h/H ₂	8	1000 °C/1.5h/H ₂	4	0.8
	1702–014							0.8
	1801–032							0.3
	1801–033							0.3
	1801–034							0.3
	1801–035							0.3
	1801–036							0.3
C11	1604–250	Ni/YSZ 65% Ni	22	1200 °C/3h/H ₂	11	1000 °C/1.5h/H ₂	4	0.8
	1604–251							
C16	1604–252	Ni/YSZ 65% Ni	22	1200 °C/3h/H ₂	16	1000 °C/1.5h/H ₂	4	0.8
	1604–253							
C24	1604–241	Ni/YSZ 65% Ni	22	1200 °C/3h/H ₂	24	1000 °C/1.5h/H ₂	4	0.8
	1604–258							
E	1801–001	Ni/YSZ 65% Ni	22	1200 °C/3h/H ₂	22	1100 °C/3h/H ₂	2	0.3
	1801–002							
	1801–003							
	1801–004							
BC16	1704–030	Ni/GDC 60% Ni	8	1100 °C/3h/H ₂	8	1100 °C/3h/H ₂	4	0.3
BC23	1704–031	Ni/GDC 60% Ni	15	1100 °C/3h/H ₂	8	1100 °C/3h/H ₂	4	0.3
BC30	1704–032	Ni/GDC 60% Ni	22	1100 °C/3h/H ₂	8	1100 °C/3h/H ₂	4	0.3

after each printing step. Then, the next printing step was conducted. For anode layer C, the wet layer thickness in series R, E, and BC was 63 μm . In the case of series E, screen printing was repeated three times with the same screen. For series C, the wet layer thickness was reduced to 21 μm and thickness variation was achieved by performing multiple printing cycles (1, 2, 3, 6, 9, and 12 cycles).

After each screen printing cycle – resulting in anode layers A, B and C with well-adjusted thicknesses – the individual anode layers were sintered separately in a batch furnace (Plansee in-house production equipment) in pure hydrogen. All sintering conditions used and the thickness of each anode layer after sintering are included in Table 2. The accuracy of the thickness measurement of anode layers B and C after sintering was $\pm 20\%$ and was mainly influenced by the rough surface of the metallic substrate and by the inhomogeneity of anode layer A, which had an average thickness of approximately 25 μm in all cell types ($\pm 20\%$ depending on substrate roughness).

Electrolyte deposition

For deposition of the electrolyte, a specific method of physical vapor deposition named gas flow sputtering (PVD-GFS) was applied. The main processing conditions can be found in Haydn et al. [16]. By providing a reactive argon-oxygen-containing atmosphere, an oxidized 8YSZ electrolyte was deposited by sputtering from a metallic Zr–Y alloy target. Thickness variation was achieved by means of a suitable adapting of deposition time, whereby decreasing the deposition time by a factor of two resulted in halving the thickness of

the electrolyte. In the present study, 2 and 4 μm thick YSZ electrolytes were prepared. For constant deposition conditions, the nominal electrolyte thickness differed by $\pm 20\%$, mainly due to inhomogeneous target abrasion during sputtering and somewhat varying deposition rates across the vacuum chamber.

After deposition of the electrolyte and the GDC-diffusion-barrier-layer, button cells with a diameter of 29.5 mm were laser cut from the larger rectangular cells. Before electrochemical testing of button cells was conducted, La_{1-x}Sr_xCo_{1-y}Fe_yO_{3- δ} (LSCF) cathode with a diameter of 9 mm (active area 0.64 mm²) was applied by screen-printing. The cathode was sintered and activated *in-situ* during heating up of the test-rig followed by a 3 h dwell time at 850 °C.

Characterization

Surface roughness

The “OGP Smartscope Flash CNC 500” optical device (Rochester, USA) was used to determine the surface roughness (Rz) according to Ref. [36]. The lateral resolution was 5 μm . The test length was 17.5 mm parallel and perpendicular to the length axis of the 100 × 140 mm² cells. The result was the mean value of the parallel and perpendicular measurements. For calculation, a Gaussian filter was applied to remove the waviness profile. To do so, the outer 2.5 mm of the measurement was excluded, resulting in a measured length of 12.5 mm (Gauss’s theory), which was further divided into 5 single sections. According to Equation (1), Rz is the average value of the sum of the highest peak and lowest

value from each single section. For a detailed explanation of the evaluation of roughness results, see relevant studies as Volk 2005 [37].

$$Rz = \sum_{i=1}^5 Rz(i) \quad (1)$$

Permeability

The permeability of the anode was measured by using the device “Dr. Wiesner Integra DFM” (Ramshalden, Germany). For measurements sintered anode layers on metal supports were used (without electrolyte). The measured area was 45 mm² and the sample was sealed using a silicone O-ring. An excess pressure of 500 hPa was applied on the anode side and the air flow rate across the porous anode structure was measured.

Leakage rate

The leakage rate of the electrolyte was measured on half-cells without cathode – i.e. after deposition of electrolyte and DB-2 – using the “Dr. Wiesner Integra DD1” device by measuring the decrease in pressure difference. The initial pressure difference was –700 hPa. The measured area was 45 mm² on button cells. The leakage rate was normalized to the measured area and a pressure difference of 100 hPa. Again, the sample was tightened using a silicon O-ring.

Electrochemical characterization

Button cells with a cell size of 29.5 mm and a cathode size of 9 mm in diameter were electrochemically characterized at Plansee SE. [Supplementary Fig. S2](#) shows the basic principle of the test rig used in this study.

To put the cells into operation, each cell was heated at 9 K/min to 450 °C, followed by a dwell time of 0.5 h for binder burn-off. During heating and debinding, air was fed to the cathode side and Ar-4% H₂ to the anode side. The sample was then further heated at 2 K/min to 600 °C. At this temperature, gas

on the anode side was changed to N₂-20% H₂, followed by another heating ramp at 1 K/min to 850 °C. At this temperature, a dwell time of 3 h enabled sealing of the glass solder and in-situ sintering of the LSCF cathode. Afterwards, the MSC was activated at 800 °C for 0.5 h by feeding pure dry hydrogen to the anode side and air to the cathode side, followed by a stabilization step in which a current density of 125 mA/cm² was applied for 1 h. During electrochemical testing, gas flow rates were kept constant at 200 ml/min air on the cathode side and 100 ml/min H₂ on the anode side. Under these conditions, fuel utilization at 0.7 V and 700 °C was at a relatively low level of approximately 6%. The risk of gas undersupply at high current densities was therefore reduced to a minimum, enabling an objective comparison of different cell architectures. I–V-curves were recorded by systematically varying the operating temperature to between 800 °C and 550 °C. To record DC data, the current rate was raised by 33 mA/min until the minimum voltage of 0.66 V was achieved.

Results and discussion

Series R

The reference cells in this work were produced in the same way as the cells developed by Rojek-Wöckner et al. [17]. In that study, a maximum current density of 0.75 A/cm² (n = 1 electrochemically tested cell) was achieved at 700 °C and 0.7 V, which was significantly lower than the current density of 1.29 ± 0.08 A/cm² (n = 3 electrochemically tested cells) measured in the present study with a nominally similar cell design (Fig. 2). The huge difference in the electrochemical performance of these nominally similar cells can be explained by several influence factors. One such factor is the difference in cell size. While in the present study the active size of the button cells was only 0.64 cm², Rojek-Wöckner et al.

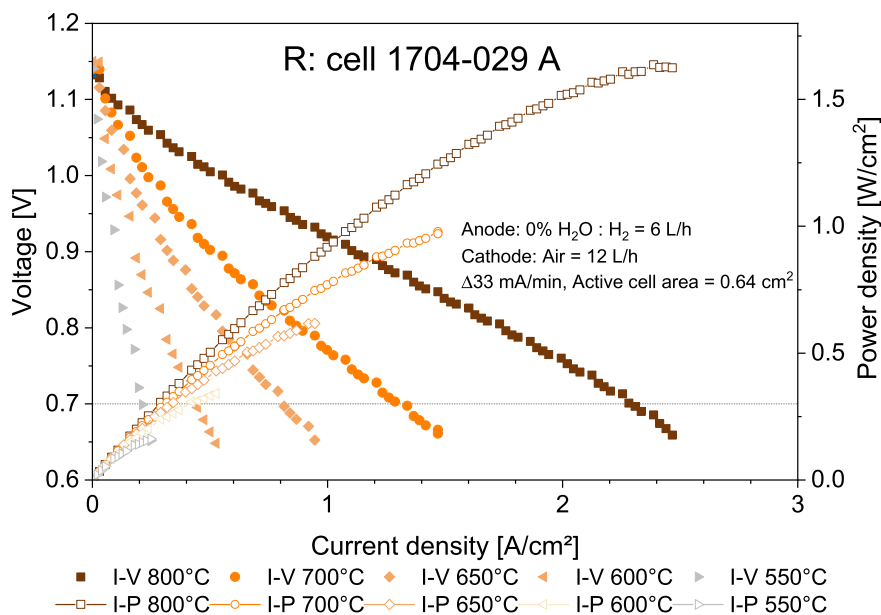


Fig. 2 – Electrochemical characterization of a series R cell acting as a reference for subsequent work. Low fuel utilization of 6% was used to reduce the influence of gas diffusion limitation to a minimum.

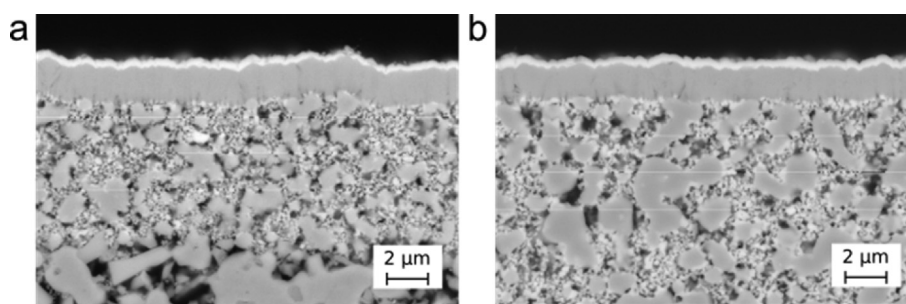


Fig. 3 – Comparison of the microstructure of anode layer C under different sintering conditions a.) 1000 °C, 1.5 h, H₂ (series C, cell-ID 1604–244) b.) 1100 °C, 3 h, H₂ (series E, cell-ID 1801–001).

used a larger cell size with an active area of 16 cm². An increase in cell size might deteriorate current collection and gas flow distribution, both of which have an impact on cell performance. Furthermore, the cells were tested in different test rigs (at Forschungszentrum Jülich and at Plansee) using varying sealing concepts. Another important impact on cell performance is the clear difference in fuel gas utilization. In the present study, the reference cells ran with a very low fuel utilization of approximately 6% at 700 °C and 0.7 V. In comparison, Rojek-Wöckner et al. operated their cells with a higher fuel utilization of around 17%. With increasing utilization, gas-diffusion becomes a more important limiting factor.

Since all characterizations involved in this study were performed on button cells only, a current density of 1.29 A/cm² at 700 °C and 0.7 V was defined as a reference value for the subsequent investigations with modified cell designs.

Series C and series E

As a starting point for further anode optimization, the sintering temperature and dwell time of layer C were reduced to 1000 °C and 1.5 h, respectively, to obtain a finer anode microstructure with an increased amount of electrochemically active area. In series C, the thickness of layer C was varied to between 4 μm and 24 μm to find the best compromise in terms of electrochemical active volume and gas diffusion limitation. In series E, a first attempt was conducted to reduce the electrolyte thickness from 4 μm to 2 μm, which is expected to lower the contribution of the electrolyte to the ohmic resistance of the cell. Moreover, a lower electrolyte thickness implies a shorter deposition time under vacuum conditions and therefore lowers cell production costs, which is thus also attractive from an economic point of view.

The impact of the sintering temperature on the microstructure of anode layer C can be seen in Fig. 3. The microstructures were characterized by image analysis using the

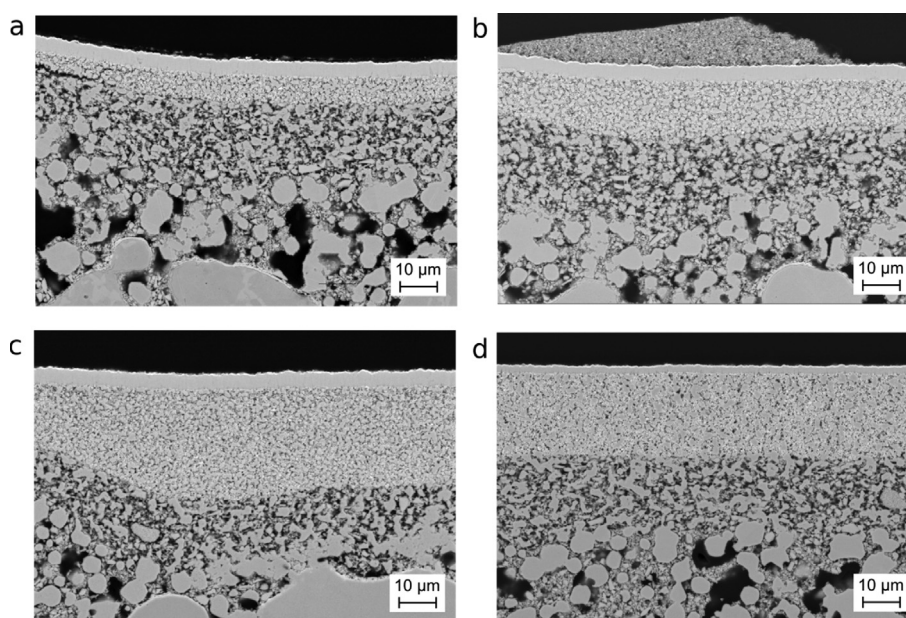


Fig. 4 – Microstructure of anode layers and electrolyte of MSCs from series C and series E a.) Anode thickness: 6 μm (C6, cell ID 1604–246) b.) Anode thickness: 11 μm (C11, cell ID 1604–251) c.) Anode thickness: 24 μm (C24, cell ID 1604–258) d.) Anode thickness: 22 μm; reduced electrolyte thickness: 2 μm (E, cell ID 1801–001).

Table 3 – Characteristic properties of MSCs from series R, C, and E. Roughness and permeability were measured before electrolyte coating. The leakage rate is related to the sputtered electrolyte, which had a thickness of 4 μm for series R and C, and a thickness of 2 μm for series E. Cell performance of C4 could not be measured due to partial delamination and high leakage rate.

Cell design	Roughness [μm]	Permeability [l/min]	Leakage rate [$\cdot 10^{-4}$ hPa l/s $\cdot\text{cm}^2$]	Open cell voltage [V]	Current density @ 700 $^{\circ}\text{C}$, 0.7 V [A/cm 2]
R	10.3 (n = 1)	1.9 (n = 1)	3.2 \pm 1.4 (n = 8)	1.12 \pm 0.02 (n = 3)	1.29 \pm 0.08 (n = 3)
C4	11.5 \pm 2.1 (n = 2)	0.8 (n = 1)	50.0 \pm 4.5 (n = 6)	n.m.	n.m.
C6	11.1 \pm 1.3 (n = 6)	n.m.	2.9 \pm 2.5 (n = 41)	1.14 \pm 0.02 (n = 5)	1.60 \pm 0.23 (n = 5)
C8	9.2 \pm 0.6 (n = 3)	n.m.	10.0 \pm 1.3 (n = 40)	1.12 \pm 0.01 (n = 2)	1.63 \pm 0.11 (n = 3)
C11	7.9 \pm 0.2 (n = 2)	0.7 (n = 1)	1.8 \pm 0.8 (n = 14)	1.10 (n = 1)	1.54 (n = 1)
C16	6.9 \pm 0.3 (n = 2)	<0.02 (n = 1)	1.9 \pm 1.1 (n = 10)	1.11 (n = 1)	1.49 (n = 1)
C24	4.8 \pm 0.5 (n = 2)	<0.02 (n = 1)	1.5 \pm 0.5 (n = 7)	1.11 (n = 1)	1.47 (n = 1)
E	7.8 \pm 0.4 (n = 4)	1.1 \pm 0.0 (n = 4)	30.0 \pm 1.3 (n = 16)	1.13 (n = 1)	1.65 (n = 1)

n = number of samples, n.m. = not measured.

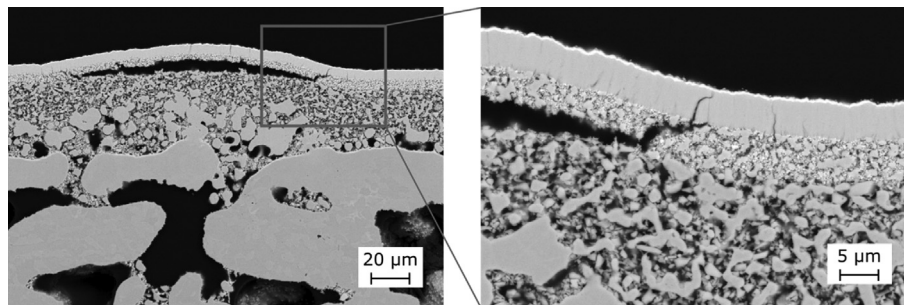


Fig. 5 – Microstructure of MSC C4 (Cell-ID 1604–242) with delamination at low C-anode thicknesses caused by the screen printing process on the rough B-subsurface. Owing to the relatively high magnification of the SEM images, this roughness (defined by DIN EN ISO 4287:2010–07), is visible as the “wave-like” unevenness of the anode surface.

linear intercept method. With this method, a porosity of $25 \pm 7\%$ was measured when sintering at $1000\text{ }^{\circ}\text{C}$ and 1.5 h. As expected, a lower porosity of $20 \pm 7\%$ was found at a higher sintering temperature of $1100\text{ }^{\circ}\text{C}$ and longer dwell time of 3 h. The pore sizes did not follow this trend. At the lower sintering temperature ($1000\text{ }^{\circ}\text{C}$, 1.5 h), the average pore size was $125 \pm 25\text{ nm}$, while at the increased sintering temperature, the pore size increased to $179 \pm 33\text{ nm}$, which might compensate for the influence of the lower porosity on the gas diffusion rate. Solid wetting effects between Ni and GDC were most probably responsible for this effect, which led to abnormal coarsening of the Ni phase in contact with GDC. Similar effects are described in the literature by several authors [38–40], but a detailed explanation of this phenomenon is lacking. The large scattering of pore size values was a result of only measuring three lines for each microstructure. Furthermore, the accuracy is dependent on selecting the appropriate greyscale settings at the interfaces.

Fig. 4 shows the microstructure of the MSCs after varying the thickness of anode layer C between $6\text{ }\mu\text{m}$ and $24\text{ }\mu\text{m}$. As the thickness of layer C increased, the roughness existing after application of anode layer A and B could be balanced out more effectively, resulting in a clear reduction in surface roughness (Table 3). Please note that the term “surface roughness” refers to the wave-like structures of the anode layer in Fig. 4 with $10\text{--}20\text{ }\mu\text{m}$ in height and approximately $100\text{ }\mu\text{m}$ in length,

which is in accordance to the definition of roughness in DIN EN ISO 4287:2010–07.

Examples of such roughness can be seen e.g. in Fig. 4 a.) and c.) on the left-hand side. In areas with increased roughness, there is a possibility that higher stresses could occur, especially during sputtering of the electrolyte. In the worst case, this could cause delamination of the weakest component (in this case the anode layer C, which was sintered at the lower temperature) due to limited mechanical strength. Our experiments also show that the risk of delamination of layer C was more pronounced at lower sintering temperatures ($1000\text{ }^{\circ}\text{C}$ vs. $1100\text{ }^{\circ}\text{C}$) and lower layer thickness – see for example cell C4 in Fig. 5. Delamination at numerous positions led to high leakage rates and cell tests were not reasonable. The delaminations occurred at places with low C-anode thicknesses combined with a convex B-subsurface. With higher anode thickness in cell type C6, the probability of delaminations already decreased but still occurred, visible for example in Fig. 4 a.), top left part. The occurrence of partial delamination is thought to be the main reason for the large scattering of leakage rates and electrochemical performance data determined of cells from the C6 group. To keep the risk of delamination at a low level, preliminary experiments involving sputtering a thin-film electrolyte with $2\text{ }\mu\text{m}$ thickness were conducted on an anode. Here, anode layer C had a thickness of $22\text{ }\mu\text{m}$ and was sintered at $1100\text{ }^{\circ}\text{C}$.

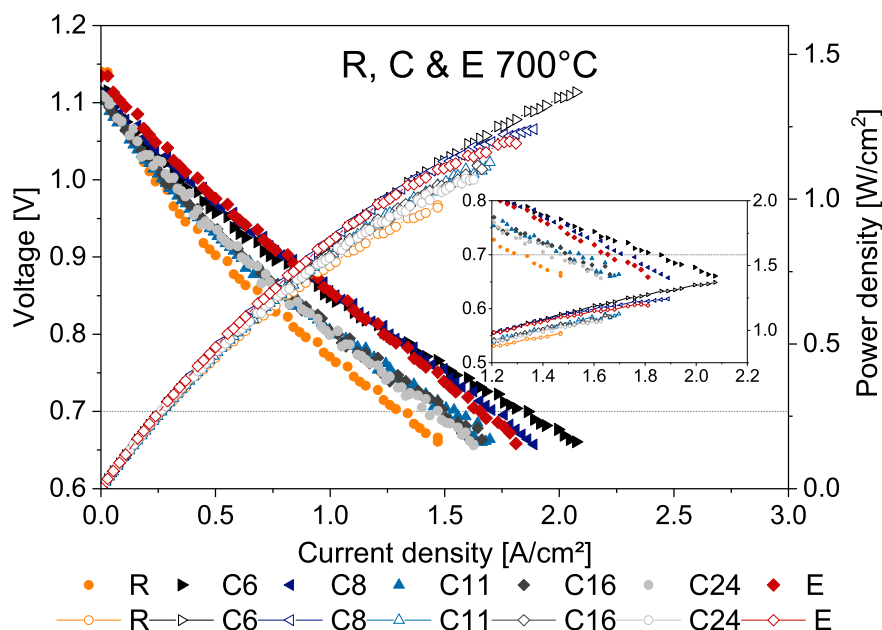


Fig. 6 – Current density–voltage curves of series R, series C, and series E cells at 700 °C (cell-IDs: R – 1704-029 A, C6 – 1604-246 D, C8 – 1702-014 F, C11 – 1604-251 E, C16 – 1604-252 C, C24 – 1604-241 F, E – 1801-001 C).

To achieve a better understanding of the influence of anode thickness on gas diffusion, permeability measurements were carried out on series R, series C, and series E before electrolyte coating (Table 3). Air was used for all permeability measurements. During real cell operation, less pronounced gas diffusion limitation is expected due to the smaller size of hydrogen molecules. The highest permeability of 1.9 l/min was achieved for series R. All samples from series C showed lower permeability, which was assumed to be caused by the lower pore size of anode layer C when sintered at 1000 °C. Not unexpectedly, permeability decreased as the layer thickness increased. The permeability of series E was also lower than the reference cells, mainly due to the greater thickness of layer C (at the same sintering temperature). Fig. 6 summarizes the electrochemical performance of series C and series E samples at a constant operation temperature of 700 °C.

Despite its higher gas permeability, the current density of series R samples was lower compared to all other samples. The most probable reason for this is the coarser microstructure caused by using a higher sintering temperature. Based on the literature [31,32], it was expected that the electrochemically active thickness would increase with increasing particle size. The higher current density of samples C6 and C8 can analogously be explained by the finer microstructure leading to an increased electrochemically active area. Therefore, the increase of active area of cells C6 and C8 has obviously a larger effect on cell performance than the larger diffusion losses due to the somewhat reduced porosity.

With increasing thickness of layer C (C11, C16, C24), a decrease in performance was observed (compared to C6 & C8). This might be caused by a more pronounced effect of the gas diffusion resistance (even at this quite low fuel gas utilization of 6%). The influence of reduced leakage rate (Table 3) seems to be negligible in this context.

From an application point of view, the results of the variations in series C are ambivalent. On the one hand, the reduction of the sintering temperature and time led to anodes with higher inner surface and thus enhanced electrochemical performance. On the other hand, this improvement came along with a significantly higher risk of cell failure due to delamination of the electrolyte. From an industrial perspective, this is a huge problem since it causes a vast uncertainty factor for cell production and operation. Therefore, the risk of delamination clearly outweighs the attractiveness of higher cell performance and it can be concluded that for an industrial cell production the route with a sintering temperature of 1100 °C and a dwell time of 3 h is clearly the method of choice. Moreover, it should be noted that an even higher performance improvement was possible by other measures without the risk of cell failure – further details will follow below.

In series E, however, reducing the electrolyte thickness to 2 μm and increasing the thickness of layer C to 22 μm were found to be effective measures in significantly raising the current density compared to the reference series R. Interestingly, the open circuit voltage of series E is equal to the reference, despite the significantly higher leakage rate. Supplementary Fig. S3 shows the current density–voltage curves in the temperature range of 550 °C–800 °C. Here, especially for the highest temperature, the shape of the curve in the high current region suggests the on-set of gas diffusion limitation.

Series BC

A promising approach for reducing the influence of gas diffusion limitation in series C-type anodes is the introduction of Ni/GDC in anode layer B as replacement for Ni/YSZ. To test the effect of a changed layer B on the gas supply

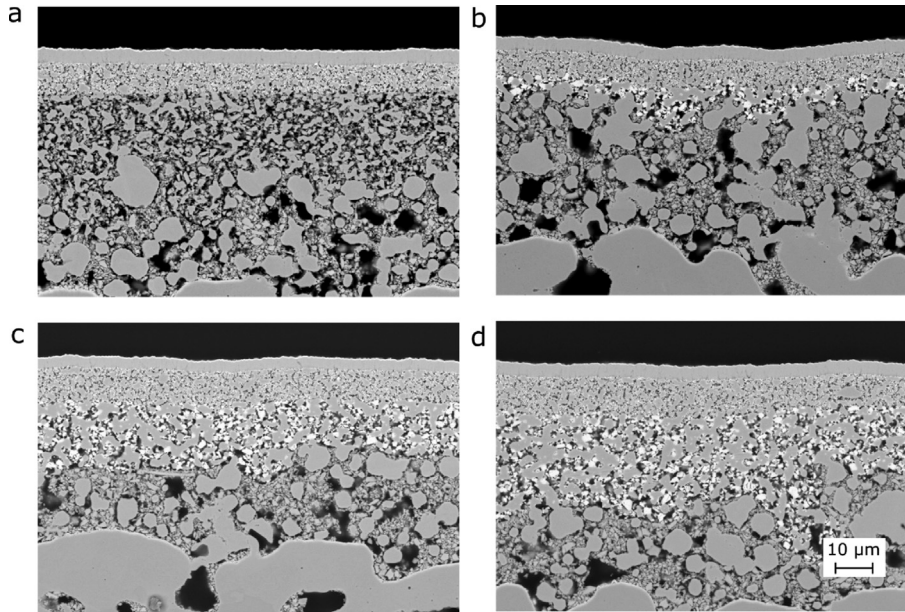


Fig. 7 – Microstructure of anode layers and electrolyte of MSCs from series R and series BC a.) Reference Ni/GDC thickness: 8 μm (R, cell ID 1704–029) b.) Total Ni/GDC thickness: 16 μm (BC16, cell ID 1704–030) c.) Total Ni/GDC thickness: 23 μm (BC23, cell ID 1704–031) d.) Total Ni/GDC thickness: 30 μm (BC30, cell ID 1704–032).

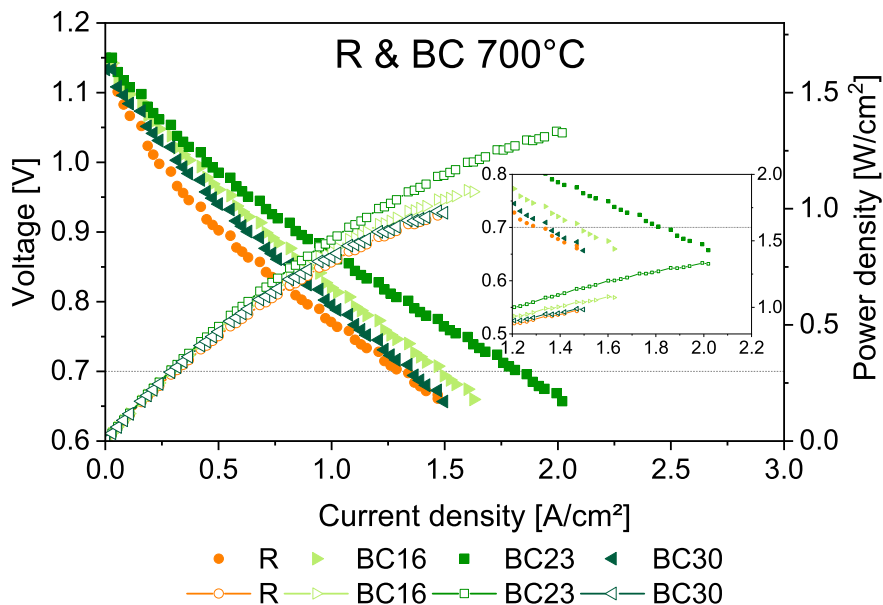


Fig. 8 – Current density–voltage curves of series R and series BC at 700 °C (cell-ID: R - 1704-029 A, BC16 - 1704-030 C, BC23 - 1704-031 B, BC30 - 1704–032 D).

Table 4 – Characteristic properties of MSCs from series BC. Again, the results are compared with series R and series E.

	Roughness [μm]	Permeability [l/min]	Leakage rate [10^{-4} hPa l/s cm^2]	Open circuit voltage @700 °C [V]	Current density @ 700 °C, 0.7 V [A/cm^2]
R	10.3 (n = 1)	1.9 (n = 1)	3.2 ± 1.4 (n = 8)	1.12 ± 0.02 (n = 3)	1.29 ± 0.08 (n = 3)
BC16	13.7 (n = 1)	2.4 (n = 1)	3.9 ± 0.8 (n = 1)	1.14 (n = 1)	1.47 (n = 1)
BC23	10.7 (n = 1)	2.4 (n = 1)	3.0 ± 1.4 (n = 1)	1.14 ± 0.01 (n = 2)	1.79 ± 0.04 (n = 2)
BC30	9.4 (n = 1)	2.1 (n = 1)	3.7 ± 2.7 (n = 1)	1.12 ± 0.01 (n = 4)	1.37 ± 0.11 (n = 4)
E	7.8 ± 0.4 (n = 4)	1.1 ± 0.0 (n = 4)	30.0 ± 12.0 (n = 16)	1.13 (n = 1)	1.65 (n = 1)

of the electrochemically active zone, three different cells were produced. They all consisted of an anode layer C with a constant thickness of 8 μm while the thickness of anode layer B was varied to 8, 15, and 22 μm (with an overall thickness of Ni/GDC of 16, 23 and 30 μm). Fig. 7 shows the related microstructures, and Fig. 8 shows the current density–voltage curves obtained at 700 °C. In series BC, the thickness of the electrolyte was kept at 4 μm since the roughness of the anode (cf. Table 4) was still in a range where sputtering of the 2 μm thick electrolyte failed, thus resulting in an unacceptably high gas leakage rate. The permeability of anodes from series BC was slightly higher than from series R, but about twice as high as from series E in which the thickness of anode layer C was 22 μm . As a consequence, despite the higher electrolyte thickness of 4 μm , the current density could be further increased. The current density from cell BC16 with 1.47 A/cm² was comparable to cell C16 (1.49 A/cm²), even though both Ni/GDC anode layers were sintered at higher temperature (1100 °C). This shows that the replacement of the coarser layer B by Ni/GDC can also offer the necessary additional active anode area without increasing the risk of electrolyte delamination. The best performing cell (BC23) reached a current density of 1.79 A/cm² at 0.7 V and 700 °C. This current density corresponds to a power density of 1.25 W/cm². In the present study, this cell was thus found to be the best compromise in terms of reliability of cell manufacturing and electrochemical performance. A preliminary conclusion on the reproducibility of cell manufacturing can be drawn from Supplementary Figs. S4 and S5. For series R and BC23, low scattering of I–V-curves hint on good reproducibility (Fig. S4). Contrarily, for cell BC30, a large scattering of electrochemical performance was obtained (Fig. S5). Here, exact cause of scattering has not yet been fully understood. The amount of cells considered in this study is not sufficient to draw conclusions, which are validated from statistical point of view. Therefore, in our future work it is planned to produce at least 10 cells with the optimum parameter set (BC23) and to test them under standardized conditions.

For use of MSCs in range extender systems, high power density in the range of 4–5 L/kW is an absolute must [2]. By implementation of the two-layer Ni/GDC configuration and use of cell type BC23, performance could be successfully increased from 0.90 W/cm² to 1.25 W/cm². Performance increase is mainly based on finding the best compromise regarding electrochemically active volume and acceptable low gas diffusion limitation.

Taking this significant increase of power density into account, the size of the MSC stack in a 30 kW fuel cell generator system can be clearly decreased. Assuming that MSCs can be assembled without loss of electrochemical performance, the number of cells can be decreased from 330 cells to 240 cells. The volume of the MSC stack (assumption 13 mL/cell) was reduced from 4.2 L to 3 L (29%). As each cell must be welded into metallic frames, additional volume can be saved by each cell. These values are only a rough estimation since on stack and system level additional performance losses are expected due to contact resistances, application of high fuel utilizations, gas flow limitations and degradation phenomena.

Conclusions

In the present study, the three-layered anode structure of the MSC concept developed by Plansee SE was systematically optimized, resulting in an increase in current density from 1.29 A/cm² to 1.79 A/cm² (+38%) at 700 °C and 0.7 V. Correspondingly, the power density was increased from 0.9 W/cm² to 1.25 W/cm². These values belong to the best electrochemical performances demonstrated for MSC technology so far. The specific progress in cell performance of the Plansee MSC was mainly based on: i.) introducing Ni/GDC as the anode material, completely replacing Ni/YSZ in the electrochemically active zone, thereby extending the electrochemically active region from only triple-phase boundaries to the entire GDC surface while additionally increasing the ionic conductivity within the electrode ii.) finding the best compromise regarding the thickness of Ni/GDC in the finely structured anode layer (layer C) and the intermediate anode layer (layer B). Furthermore, a reduction in electrolyte thickness from the current standard of 4 μm –2 μm was demonstrated, which is attractive in terms of further reduce the ohmic resistance of the MSC. Nevertheless, there are still options for further improvement. Firstly, combining reduced electrolyte thickness with novel BC anode structure is an open task. Secondly, we demonstrated recently that replacing La_{1-x}Sr_xCo_{1-y}Fe_yO_{3- δ} (LSCF) by La_{1-x}Sr_xCo_{1-y}O_{3- δ} (LSC) as cathode material is another effective measure for increasing the cell performance [35,41].

Acknowledgements

Parts of this study were conducted in cooperation with the Christian Doppler Laboratory for Interfaces in Metal-Supported Electrochemical Energy Converters. Christian Doppler Laboratories are funded in equal shares by the public authorities and the companies directly involved in the laboratories. The most important funding source of the public authorities is the Austrian Federal Ministry for Digital and Economic Affairs (BMDW). This funding is gratefully acknowledged.

Appendix A Supplementary data

Supplementary data to this article can be found online at <https://doi.org/10.1016/j.ijhydene.2019.10.010>.

REFERENCES

- [1] Rechberger J, Kaupert A, Hagerskans J, Blum L. Demonstration of the first european SOFC APU on a heavy duty truck. *Transp Res Procedia* 2016;14:3676–85. <https://doi.org/10.1016/j.trpro.2016.05.442>.
- [2] Lawlor V, Reissig M, Makinson J, Rechberger J. SOFC system for battery electric vehicle range extension: results of the first half of the mestrex project. *ECS Trans* 2017;78:191–5. <https://doi.org/10.1149/07801.0191ecst>.

- [3] Nissan unveils world's first Solid-Oxide Fuel Cell vehicle - Nissan Online Newsroom n.d. <https://nissannews.com/en-US/nissan/usa/releases/nissan-unveils-world-s-first-solid-oxide-fuel-cell-vehicle> (accessed November 1, 2018).
- [4] Brandon NP, Corcoran D, Cummins D, Duckett A, El-Khoury K, Haigh D, et al. Development of metal supported solid oxide fuel cells for operation at 500–600 °C. *J Mater Eng Perform* 2004;22:2900–3. <https://doi.org/10.1007/s11665-013-0716-7>.
- [5] Leah R, Bone A, Hammer E, Selcuk A, Rahman M, Clare A, et al. Development progress on the Ceres power steel cell technology platform: further progress towards commercialization. *ECS Trans* 2017;78:87–95.
- [6] Dogdibegovic E, Wang R, Lau GY, Tucker MC. High performance metal-supported solid oxide fuel cells with infiltrated electrodes. *J Power Sources* 2019;411:91–8. <https://doi.org/10.1016/j.jpowsour.2018.11.004>.
- [7] Tucker MC. Development of high power density metal-supported solid oxide fuel cells. *Energy Technol* 2017;5:2175–81. <https://doi.org/10.1002/ente.201700242>.
- [8] Nielsen J, Persson ÅH, Muhl TT, Brodersen K. Towards high power density metal supported solid oxide fuel cell for mobile applications. *J Electrochem Soc* 2018;165:F90–6. <https://doi.org/10.1149/2.0741802jes>.
- [9] Blennow P, Hjelm J, Klemensø T, Ramousse S, Kromp A, Leonide A, et al. Manufacturing and characterization of metal-supported solid oxide fuel cells. *J Power Sources* 2011;196:7117–25. <https://doi.org/10.1016/j.jpowsour.2010.08.088>.
- [10] Li K, Wang X, Jia L, Yan D, Pu J, Chi B, et al. High performance Ni-Fe alloy supported SOFCs fabricated by low cost tape casting-screen printing-cofiring process. *Int J Hydrogen Energy* 2014;39:19747–52. <https://doi.org/10.1016/j.ijhydene.2014.09.146>.
- [11] Zhou Y, Xin X, Li J, Ye X, Xia C, Wang S, et al. Performance and degradation of metal-supported solid oxide fuel cells with impregnated electrodes. *Int J Hydrogen Energy* 2014;39:2279–85. <https://doi.org/10.1016/j.ijhydene.2013.11.086>.
- [12] Hwang CS, Tsai CH, Hwang TJ, Chang CL, Yang SF, Lin JK. Novel metal substrates for high power metal-supported solid oxide fuel cells. *Fuel Cells* 2016;16:244–51. <https://doi.org/10.1002/face.201500216>.
- [13] Tucker MC. Progress in metal-supported solid oxide fuel cells: a review. *J Power Sources* 2010;195:4570–82. <https://doi.org/10.1016/j.jpowsour.2010.02.035>.
- [14] Krishnan V. Recent developments in metal-supported solid oxide fuel cells. *WIREs Energy Env* 2017;6:1–35. <https://doi.org/10.1002/wene.246>.
- [15] Vieweger S, Mücke R, Menzler NH, Buchkremer HP. Thin electrolytes on metal-supported fuel cells. *Fuel Cells* 2013;13:556–64. <https://doi.org/10.1002/face.201200166>.
- [16] Haydn M, Ortner K, Franco T, Uhlenbruck S, Menzler NH, Stöver D, et al. Multi-layer thin-film electrolytes for metal supported solid oxide fuel cells. *J Power Sources* 2014;256:52–60. <https://doi.org/10.1016/j.jpowsour.2014.01.043>.
- [17] Rojek-Wöckner VA, Opitz AK, Brandner M, Mathé J, Bram M. A novel Ni/ceria-based anode for metal-supported solid oxide fuel cells. *J Power Sources* 2016;328:65–74. <https://doi.org/10.1016/j.jpowsour.2016.07.075>.
- [18] Chueh WC, Hao Y, Jung W, Haile SM. High electrochemical activity of the oxide phase in model ceria-Pt and ceria-Ni composite anodes. *Nat Mater* 2012;11:155–61. <https://doi.org/10.1038/nmat3184>.
- [19] Sumi H, Shimada H, Yamaguchi Y, Yamaguchi T. Effect of anode thickness on polarization resistance for metal-supported microtubular solid oxide fuel cells. *J Electrochem Soc* 2017;164:F243–7. <https://doi.org/10.1149/2.0431704jes>.
- [20] Suzue Y, Shikazono N, Kasagi N. Micro modeling of solid oxide fuel cell anode based on stochastic reconstruction. *J Power Sources* 2008;184:52–9. <https://doi.org/10.1016/j.jpowsour.2008.06.029>.
- [21] Miyawaki K, Kishimoto M, Iwai H, Saito M, Yoshida H. Comprehensive understanding of the active thickness in solid oxide fuel cell anodes using experimental, numerical and semi-analytical approach. *J Power Sources* 2014;267:503–14. <https://doi.org/10.1016/j.jpowsour.2014.05.112>.
- [22] Hussain MM, Li X, Dincer I. A numerical investigation of modeling an SOFC electrode as two finite layers. *Int J Hydrogen Energy* 2009;34:3134–44. <https://doi.org/10.1016/j.ijhydene.2009.01.049>.
- [23] Kishimoto M, Iwai H, Saito M, Yoshida H. Characteristic length of oxide-ion conduction for prediction of active thickness in SOFC anode. *ECS Trans* 2013;57:2515–25. <https://doi.org/10.1149/05701.2515ecst>.
- [24] Zheng K, Li L, Ni M. Investigation of the electrochemical active thickness of solid oxide fuel cell anode. *Int J Hydrogen Energy* 2014;39:12904–12. <https://doi.org/10.1016/j.ijhydene.2014.06.108>.
- [25] Cai Q, Adjiman CS, Brandon NP. Investigation of the active thickness of solid oxide fuel cell electrodes using a 3D microstructure model. *Electrochim Acta* 2011;56:10809–19. <https://doi.org/10.1016/j.electacta.2011.06.105>.
- [26] Adler SB. Limitations of charge-transfer models for mixed-conducting oxygen electrodes. *Solid State Ion* 2000;135:603–12. [https://doi.org/10.1016/S0167-2738\(00\)00423-9](https://doi.org/10.1016/S0167-2738(00)00423-9).
- [27] Adler SB, Lane JA, Steele BCH. Electrode kinetics of porous mixed-conducting oxygen electrodes. *J Electrochem Soc* 1996;143:3554–63. <https://doi.org/10.1149/1.1837252>.
- [28] Deng H, Zhou M, Abeles B. Diffusion-reaction in mixed ionic electronic conductor solid oxide membranes with porous electrodes. *Solid State Ionics* 1994;74:75–84. <https://doi.org/10.1557/proc-369-415>.
- [29] Gerstl M, Hutterer A, Fleig J, Bram M, Opitz AK. Model composite microelectrodes as a pathfinder for fully oxidic SOFC anodes. *Solid State Ion* 2016;298:1–8. <https://doi.org/10.1016/j.ssi.2016.10.013>.
- [30] Nakamura T, Yashiro K, Kaimai A, Otake T, Sato K, Kawada T, et al. Determination of the reaction zone in gadolinia-doped ceria anode for solid oxide fuel cell. *J Electrochem Soc* 2008;155:B1244–50. <https://doi.org/10.1149/1.2975322>.
- [31] Wu C, Yang Z, Huo S, Najmi AUH, Du Q, Jiao K. Modeling and optimization of electrode structure design for solid oxide fuel cell. *Int J Hydrogen Energy* 2018;43:14648–64. <https://doi.org/10.1016/j.ijhydene.2018.05.152>.
- [32] Dierickx S, Mundloch T, Weber A, Ivers-Tiffée E. Advanced impedance model for double-layered solid oxide fuel cell cermet anodes. *J Power Sources* 2019;415:69–82. <https://doi.org/10.1016/j.jpowsour.2019.01.043>.
- [33] Chan SH, Xia ZT. Anode micro model of solid oxide fuel cell. *J Electrochem Soc* 2001;148:A388–94. <https://doi.org/10.1149/1.1357174>.
- [34] Rüttinger M, Mücke R, Franco T. Metal-supported cells with comparable performance to anode-supported cells in short-term stack. *Environment* 2011;35:259–68.
- [35] Udomsilp D, Roehrens D, Menzler NH, Bischof C, de Haart LGJ, Opitz AK, et al. High-performance metal-supported solid oxide fuel cells by advanced cathode processing. *J Electrochem Soc* 2017;164:F1375–84. <https://doi.org/10.1149/2.0571713jes>.
- [36] DIN EN ISO 4287. 2010-07 Geometrical Product Specifications (GPS) – surface texture: profile method – terms, Definitions

- and Surface texture parameters. ISO 2010. <https://doi.org/10.1007/s00738-009-0685-2>. ISO 4287:1997 + Cor 1:1998 + Cor 2:2005 + Amd 1:2009.
- [37] Volk R. *Rauheitsmessung: theorie und Praxis*. Berlin: Beuth; 2005.
- [38] Matsui T, Eguchi K, Shirai K, Okanishi T, Muroyama H, Eguchi K. New design concept of Ni-Doped-Ceria cermet anode for solid oxide fuel cells: redox-induced self-modification. *ECS Trans* 2017;78:1115–23. <https://doi.org/10.1149/07801.1115ecst>.
- [39] Jiao Z, Shikazono N. Study on nickel morphological change at active three-phase-boundary in solid oxide fuel cell anode using patterned nickel-film electrode. *ECS Trans* 2017;78:1169–77. <https://doi.org/10.1149/07801.1169ecst>.
- [40] Sciazko A, Jiao Z, Miyahara K, Komatsu Y, Shikazono N, Shimura T. Influence of initial powder morphology on polarization characteristics of nickel/gadolinium-doped-ceria solid oxide fuel cells electrode. *J Electrochem Soc* 2019;166:44–52. <https://doi.org/10.1149/2.0181902jes>.
- [41] Udomsilp D, Thaler F, Menzler NH, Bischof C, de Haart LGJ, Opitz AK, et al. Dual-phase cathodes for metal-supported solid oxide fuel cells – processing, performance, durability. *J Electrochem Soc* 2019;166:F506–10. <https://doi.org/10.1149/2.0561908jes>.